

1

2 Modular strategies for spatial mapping of 3 multi-modal mouse brain data

4 Nicholas J. Tustison¹, Min Chen², Fae N. Kronman³, Jeffrey T. Duda², Clare Gamlin⁴, Mia
5 G. Tustison, Michael Kunst⁴, Rachel Dalley⁴, Staci Sorenson⁴, Quanxin Wang⁴, Lydia Ng⁴,
6 Yongsoo Kim³, and James C. Gee²

7 ¹Department of Radiology and Medical Imaging, University of Virginia, Charlottesville, VA

8 ²Department of Radiology, University of Pennsylvania, Philadelphia, PA

9 ³Department of Neural and Behavioral Sciences, Penn State University, Hershey, PA

10 ⁴Allen Institute for Brain Science, Seattle, WA

11

12 Corresponding authors:

13

14 Nicholas J. Tustison, DSc

15 Department of Radiology and Medical Imaging

16 University of Virginia

17 ntustison@virginia.edu

18

19 James C. Gee, PhD

20 Department of Radiology

21 University of Pennsylvania

22 gee@upenn.edu

²³ **Abstract**

²⁴ Large-scale efforts by the BRAIN Initiative Cell Census Network (BICCN) are generating
²⁵ a comprehensive reference atlas of cell types in the mouse brain. A key challenge in this
²⁶ effort is mapping diverse datasets, acquired with varied imaging, tissue processing, and
²⁷ profiling methods, into shared coordinate frameworks. Here, we present modular mapping
²⁸ pipelines developed using the Advanced Normalization Tools Ecosystem (ANTsX) to align
²⁹ MERFISH spatial transcriptomics and high-resolution fMOST morphology data to the Allen
³⁰ Common Coordinate Framework (CCFv3), and developmental MRI and LSFM data to the
³¹ Developmental CCF (DevCCF). Simultaneously, we introduce two novel methods: 1) a
³² velocity field-based approach for continuous interpolation across developmental timepoints,
³³ and 2) a deep learning framework for automated brain parcellation using minimally annotated
³⁴ and publicly available data. All workflows are open-source and reproducible. We also provide
³⁵ general guidance for selecting appropriate strategies across modalities, enabling researchers
³⁶ to adapt these tools to new data.

³⁷ 1 Introduction

³⁸ Over the past decade, there have been significant advancements in mesoscopic single-cell
³⁹ analysis of the mouse brain. It is now possible to track single neurons¹, observe whole-
⁴⁰ brain developmental changes at cellular resolution², associate brain regions with genetic
⁴¹ composition³, and locally characterize neural connectivity⁴. These scientific achievements have
⁴² been propelled by high-resolution profiling and imaging techniques that enable submicron,
⁴³ multimodal, three-dimensional characterizations of whole mouse brains. Among these are
⁴⁴ micro-optical sectioning tomography^{5,6}, tissue clearing methods^{1,7}, spatial transcriptomics^{8,9},
⁴⁵ and single-cell genomic profiling¹⁰, each offering expanded specificity and resolution for
⁴⁶ cell-level brain analysis.

⁴⁷ Recent efforts by the NIH BRAIN Initiative have mobilized large-scale international col-
⁴⁸ laborations to create a comprehensive reference database of mouse brain structure and
⁴⁹ function. The BRAIN Initiative Cell Census Network has aggregated over 40 multimodal
⁵⁰ datasets from more than 30 research groups¹¹, many of which are registered to standardized
⁵¹ anatomical coordinate systems to support integrated analysis. Among the most widely used
⁵² of these frameworks is the Allen Mouse Brain Common Coordinate Framework (CCFv3)¹².
⁵³ Other CCFs include modality-specific references^{13–15} and developmental atlases^{16,17} that track
⁵⁴ structural change across time.

⁵⁵ 1.1 Mouse brain mapping challenges

⁵⁶ Robust mapping of cell type data into CCFs is essential for integrative analysis of morphology,
⁵⁷ connectivity, and molecular identity. However, each modality poses unique challenges. For
⁵⁸ example, differences in tissue processing, imaging protocols, and anatomical completeness
⁵⁹ often introduce artifacts such as distortion, tearing, holes, and signal dropout^{18–23}. Intensity
⁶⁰ differences and partial representations of anatomy can further complicate alignment. Given
⁶¹ this diversity specialized strategies are often needed to address the unique, modality-specific
⁶² challenges.

⁶³ Existing mapping solutions fall into three broad categories. The first includes integrated

64 processing platforms that provide users with mapped datasets (e.g., Allen Brain Cell Atlas²⁴,
65 Brain Architecture Portal²⁵, OpenBrainMap²⁶, and Image and Multi-Morphology Pipeline²⁷).
66 These offer convenience and high-quality curated data, but limited generalizability and
67 customization. The second category involves highly specialized pipelines tailored to specific
68 modalities such as histology^{28–30}, magnetic resonance imaging (MRI)^{31–33}, microCT^{34,35}, light
69 sheet fluorescence microscopy (LSFM)^{36,37}, fluorescence micro-optical sectioning tomography
70 (fMOST)^{15,38}, and spatial transcriptomics, including multiplexed error-robust fluorescence in
71 situ hybridization (MERFISH)^{39–41}. While effective, these solutions often require extensive
72 engineering effort to adapt to new datasets or modalities. Finally, general-purpose toolkits
73 such as elastix⁴², Slicer3D⁴³, and the Advanced Normalization Tools Ecosystem (ANTsX)⁴⁴
74 have all been applied to mouse brain mapping scenarios (e.g., SlicerMEMOS⁴⁵). These
75 toolkits support modular workflows that can be flexibly composed from reusable components,
76 offering a powerful alternative to rigid, modality-specific solutions. However, their use often
77 requires familiarity with pipeline modules, parameter tuning, and tool-specific conventions
78 which can limit adoption.

79 Building on this third category, we describe a set of modular, ANTsX-based pipelines
80 specifically tailored for mapping diverse mouse brain data into standardized anatomical
81 frameworks. These include two new pipelines: a velocity field-based interpolation model that
82 potentially enables biologically plausible transformations across developmental timepoints, and
83 a template-based deep learning pipeline for brain extraction and parcellation requiring minimal
84 annotated data. In addition, we include two modular pipelines for aligning multiplexed
85 error-robust fluorescence in situ hybridization (MERFISH) and fMOST datasets to the
86 Allen CCFv3. These workflows were adapted and tailored using ANTsX tools to support
87 collaborative efforts within the BICCN and are now made openly available in a reproducible
88 format. To facilitate broader adoption, we also provide general guidance for customizing
89 these strategies across imaging modalities and data types. We first introduce key components
90 of the ANTsX toolkit, which provide a basis for all of the mapping workflows described here,
91 and then detail the specific contributions made in each pipeline.

92 1.2 The Advanced Normalization Tools Ecosystem (ANTsX)

93 The Advanced Normalization Tools Ecosystem (ANTsX) has been used in a number of
94 applications for mapping mouse brain data as part of core processing steps in various
95 workflows^{30,46–49}, particularly its pairwise, intensity-based image registration capabilities⁵⁰
96 and bias field correction⁵¹. Historically, ANTsX development is based on foundational
97 approaches to image mapping^{52–54}, especially in the human brain, with key contributions such
98 as the Symmetric Normalization (SyN) algorithm⁵⁰. It has been independently evaluated in
99 diverse imaging domains including multi-site brain MRI⁵⁵, pulmonary CT⁵⁶, and multi-modal
100 brain tumor registration⁵⁷.

101 Beyond registration, ANTsX provides functionality for template generation⁵⁸, intensity-based
102 segmentation⁵⁹, preprocessing^{51,60}, and deep learning⁴⁴. It has demonstrated strong perfor-
103 mance in consensus labeling⁶¹, brain tumor segmentation⁶², and cardiac motion estimation⁶³.
104 Built on the Insight Toolkit (ITK)⁶⁴, ANTsX benefits from open-source contributions while
105 supporting continued algorithm evaluation and innovation. In the context of mouse brain
106 data, ANTsX provides a robust platform for developing modular pipelines to map diverse
107 imaging modalities into CCFs. This paper highlights its use across distinct BICCN projects
108 such as spatial transcriptomic data from MERFISH, structural data from fMOST, and
109 multimodal developmental data from LSFM and MRI. We describe both shared infrastructure
110 and targeted strategies adapted to the specific challenges of each modality.

111 1.3 Novel ANTsX-based open-source contributions

112 We introduce two novel contributions to ANTsX developed as part of collabortive efforts in
113 creating the Developmental Common Coordinate Framework (DevCCF)¹⁶. First, we present
114 an open-source velocity field-based interpolation framework for continuous mapping across the
115 sampled embryonic and postnatal stages of the DevCCF atlas¹⁶. This functionality enables
116 biologically plausible interpolation between timepoints via a time-parameterized diffeomorphic
117 velocity model⁶⁵, inspired by previous work⁶⁶. Second, we present a deep learning pipeline for
118 structural parcellation of the mouse brain from multimodal MRI data. This includes two novel

¹¹⁹ components: 1) a template-derived brain extraction model using augmented data from two
¹²⁰ ANTsX-derived template datasets^{67,68}, and 2) a template-derived parcellation model trained
¹²¹ on DevCCF P56 labelings mapped from the AllenCCFv3. This pipeline demonstrates how
¹²² ANTsX tools and public resources can be leveraged to build robust anatomical segmentation
¹²³ pipelines with minimal annotated data. We independently evaluate this framework using a
¹²⁴ longitudinal external dataset⁶⁹, demonstrating generalizability across specimens and imaging
¹²⁵ protocols. All components are openly available through the R and Python ANTsX packages,
¹²⁶ with general-purpose functionality documented in a reproducible, cross-platform tutorial
¹²⁷ (<https://tinyurl.com/antsxtutorial>). Code specific to this manuscript, including scripts to
¹²⁸ reproduce the novel contributions and all associated evaluations, is provided in a dedicated
¹²⁹ repository (<https://github.com/ntustison/ANTsXMouseBrainMapping>). Additional tools for
¹³⁰ mapping spatial transcriptomic (MERFISH) and structural (fMOST) data to the AllenCCFv3
¹³¹ are separately available at (<https://github.com/dontminchenit/CCFAlignmentToolkit>).

132 **2 Results**

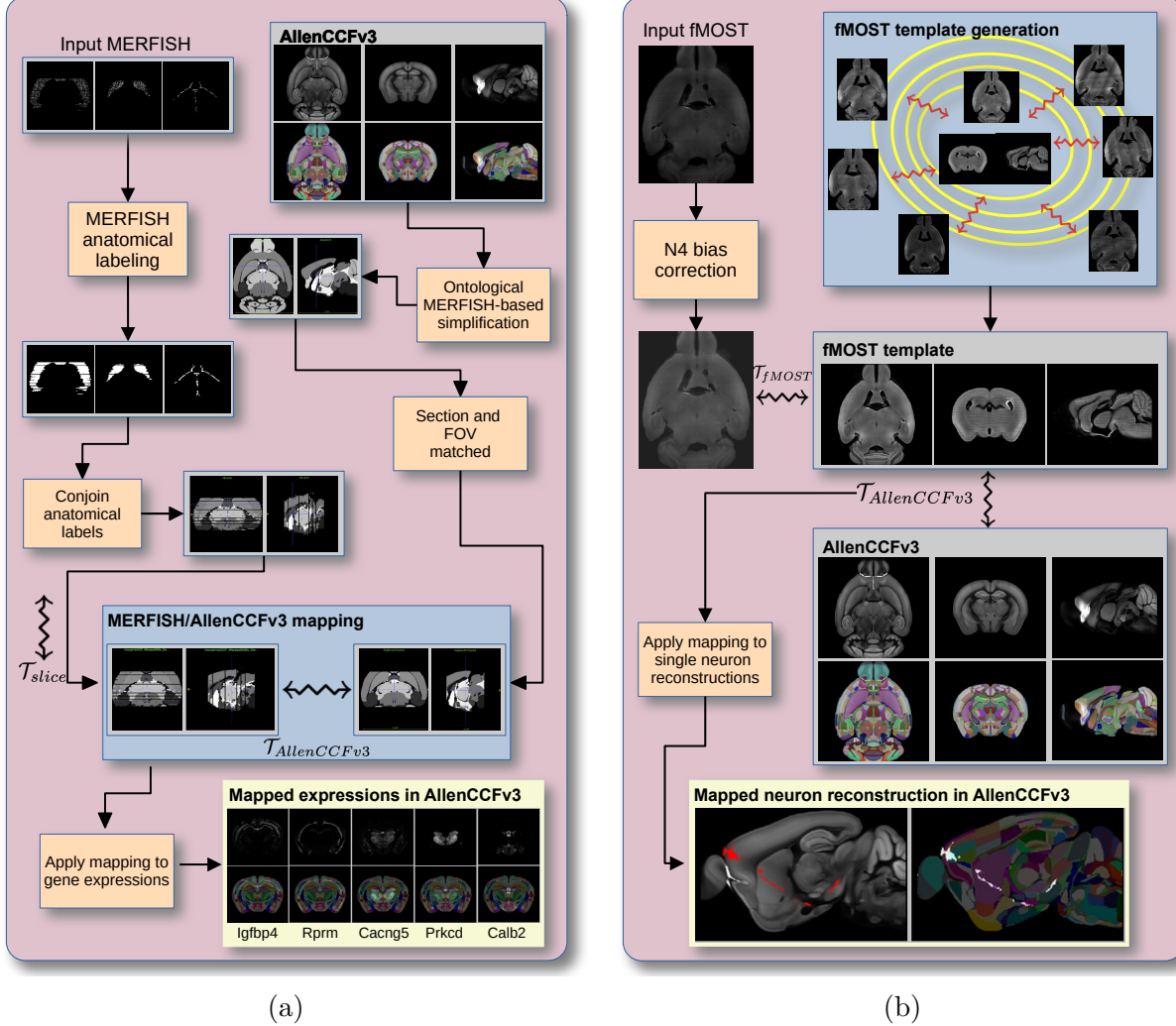


Figure 1: Diagram of the two ANTsX-based pipelines for mapping (a) MERFISH and (b)fMOST data into the space of AllenCCFv3. Each generates the requisite transforms, \mathcal{T} , to map individual images to the CCF.

133 **2.1 AllenCCFv3 brain image mapping**

134 **2.1.1 Mapping multiplexed error-robust fluorescence *in situ* hybridization
135 (MERFISH) data**

136 **Overview.** We developed an ANTsX-based pipeline to map spatial transcriptomic MERFISH
137 data into the AllenCCFv3 (Figure 1(a)). This approach was used in recent efforts to create a

138 high-resolution transcriptomic atlas of the mouse brain⁴⁹. The pipeline maps spatial gene
139 expression patterns from MERFISH onto anatomical labels in the AllenCCFv3. It includes
140 MERFISH-specific preprocessing steps such as section reconstruction, label generation from
141 spatial transcriptomic maps, and anatomical correspondence mapping. Alignment proceeds
142 in two stages: 1) 3D affine registration and section matching of the AllenCCFv3 to the
143 MERFISH data, and 2) linear + deformable 2D section-wise alignment between matched
144 MERFISH and atlas slices. These transformations are concatenated to produce a complete
145 mapping from each MERFISH data to AllenCCFv3.

146 **Data.** MERFISH imaging was performed on cryosectioned brains from C57BL/6 mice using
147 previously described protocols⁴⁹. Brains were placed into an optimal cutting temperature
148 (OCT) compound (Sakura FineTek 4583) stored at -80°. The fresh frozen brain was sectioned
149 at 10 μm on Leica 3050 S cryostats at intervals of 200 μm to evenly cover the brain. A set
150 of 500 genes was selected to distinguish \sim 5200 transcriptomic clusters. Raw MERSCOPE
151 data were decoded using Vizgen software (v231). Cell segmentation was performed using
152 Cellpose^{70,71} based on DAPI and PolyT stains which was propagated to adjacent slices across
153 z-planes. Each MERFISH cell was assigned a transcriptomic identity by mapping to a
154 scRNA-seq reference taxonomy.

155 **Evaluation.** Alignment quality was evaluated iteratively by an expert anatomist, guided
156 by expected gene-marker correspondences to AllenCCFv3 regions. As previously reported⁴⁹,
157 of the 554 terminal gray matter regions in the AllenCCFv3, only seven small subregions
158 were not represented in the MERFISH dataset: frontal pole layer 1 (FRP1), FRP2/3, FRP5;
159 accessory olfactory bulb glomerular (AOBgl), granular (AOBgr), and mitral (AOBmi) layers;
160 and the accessory supraoptic group (ASO).

161 2.1.2 Mapping fluorescence micro-optical sectioning tomography (fMOST) data

162 **Overview.** We also constructed a pipeline for mapping fMOST images to the AllenCCFv3
163 using ANTsX (Figure 1(b)). The approach leverages a modality-specific average fMOST
164 atlas as an intermediate target, adapted from previous work in human and mouse brain
165 mapping^{12,15,16,58,72–75}. The atlas was constructed from 30 fMOST images selected to capture

¹⁶⁶ representative variability in anatomical shape and image intensity across the population.
¹⁶⁷ Preprocessing includes cubic B-spline downsampling to match the $25\text{ }\mu\text{m}$ isotropic AllenCCFv3
¹⁶⁸ resolution, stripe artifact suppression using a 3D notch filter implemented with SciPy's
¹⁶⁹ frequency-domain filtering tools, and N4 bias field correction⁵¹. A one-time, annotation-
¹⁷⁰ driven alignment registers the fMOST atlas to AllenCCFv3 using landmark-based registration
¹⁷¹ of key structures. This canonical mapping is then reused. New fMOST specimens are first
¹⁷² aligned to the fMOST atlas using standard intensity-based registration, and the concatenated
¹⁷³ transforms yield full spatial normalization to the AllenCCFv3. This same mapping can be
¹⁷⁴ applied to neuron reconstructions to facilitate population-level analysis of morphology and
¹⁷⁵ spatial distribution.

¹⁷⁶ **Data.** fMOST imaging was performed on 55 mouse brains with sparse transgenic labeling of
¹⁷⁷ neuron populations^{76,77} using the high-throughput fMOST platform^{78,79}. Voxel resolution was
¹⁷⁸ $0.35 \times 0.35 \times 1.0\text{ }\mu\text{m}^3$. Two imaging channels were acquired: GFP-labeled neuron morphology
¹⁷⁹ (green), and propidium iodide counterstaining for cytoarchitecture (red). Alignment was
¹⁸⁰ performed using the red channel for its greater contrast, though multi-channel mapping is
¹⁸¹ also supported.

¹⁸² **Evaluation.** The canonical mapping from the fMOST atlas to AllenCCFv3 was evaluated
¹⁸³ using both quantitative and qualitative approaches. Dice similarity coefficients were computed
¹⁸⁴ between corresponding anatomical labels in the fMOST atlas and AllenCCFv3 following
¹⁸⁵ registration. These labels were manually annotated or adapted from existing atlas segmen-
¹⁸⁶ tations. Representative Dice scores included: whole brain (0.99), caudate putamen (0.97),
¹⁸⁷ fimbria (0.91), posterior choroid plexus (0.93), anterior choroid plexus (0.96), optic chiasm
¹⁸⁸ (0.77), and habenular commissure (0.63). In addition to these quantitative assessments,
¹⁸⁹ each registered fMOST specimen was evaluated qualitatively. An expert anatomist reviewed
¹⁹⁰ alignment accuracy and confirmed structural correspondence. Neuron reconstructions from
¹⁹¹ individual brains were also transformed into AllenCCFv3 space, and their trajectories were
¹⁹² visually inspected to confirm anatomical plausibility and preservation of known projection
¹⁹³ patterns.

¹⁹⁴ 2.2 Continuously mapping the DevCCF developmental trajectory

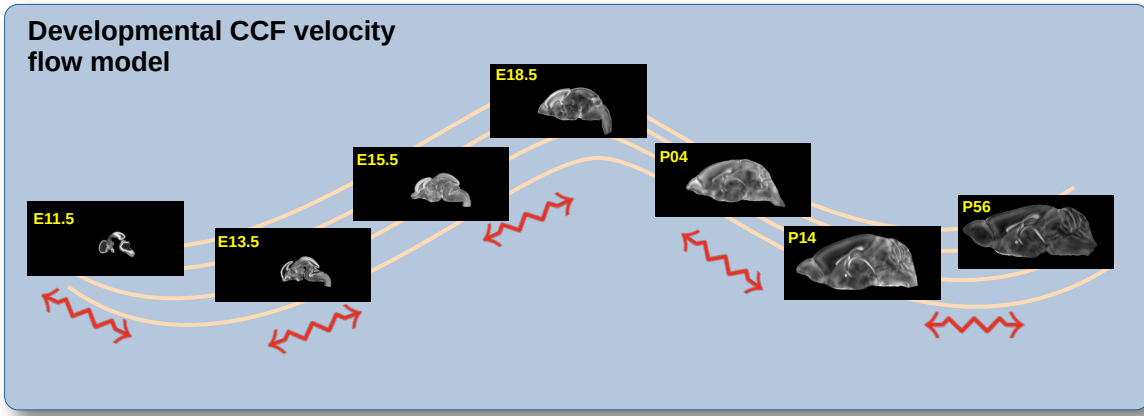


Figure 2: The spatial transformation between any two time points within the continuous DevCCF longitudinal developmental trajectory is available through the use of ANTsX functionality for generating a velocity flow model.

¹⁹⁵ The DevCCF is an openly accessible resource for the mouse brain research community⁸⁰,
¹⁹⁶ comprising symmetric, multi-modal MRI and LSFM templates generated using the ANTsX
¹⁹⁷ framework⁵⁸. It spans key stages of mouse brain development (E11.5, E13.5, E15.5, E18.5,
¹⁹⁸ P4, P14, and P56) and includes structural labels defined by a developmental ontology. The
¹⁹⁹ DevCCF was constructed in coordination with the AllenCCFv3 to facilitate integration across
²⁰⁰ atlases and data types.

²⁰¹ Although this collection provides broad developmental coverage, its discrete sampling
²⁰² limits the ability to model continuous transformations across time. To address this,
²⁰³ we developed a velocity flow-based modeling approach that enables anatomically plau-
²⁰⁴ sible, diffeomorphic transformations between any two continuous time points within
²⁰⁵ the DevCCF range. This functionality is implemented in both ANTsR and ANTsPy
²⁰⁶ (`ants.fit_time_varying_transform_to_point_sets(...)`) and integrates seamlessly with
²⁰⁷ existing ANTsX workflows. The velocity field is encoded as a 4D ITK image where each
²⁰⁸ voxel stores the x,y,z components of motion at a given time point.

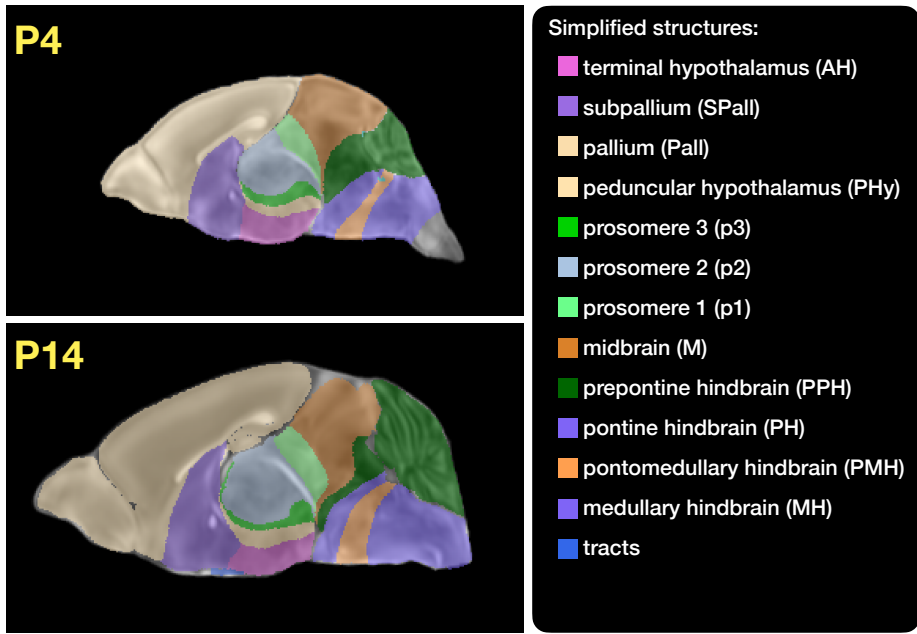


Figure 3: Annotated regions representing common labels across developmental stages, shown for both P4 and P14.

209 2.2.1 Data

210 Each DevCCF template includes over 2,500 labeled anatomical regions, with spatial resolutions
211 ranging from 31.5 to $50\mu\text{m}$. For the velocity flow modeling task, we identified a common set
212 of 26 bilateral regions (13 per hemisphere) that were consistently labeled across all timepoints.
213 These regions span major developmental domains including the pallium, subpallium, midbrain,
214 prosomeres, hypothalamus, hindbrain subregions, and key white matter tracts (Figure 3).

215 Prior to velocity field optimization, all templates were rigidly aligned to the DevCCF
216 P56 template using the centroids of these common label sets. Pairwise correspondence
217 between adjacent timepoints was then computed using ANTsX’s multi-metric registration
218 via `ants.registration(...)`. Instead of performing intensity-based multi-label registration
219 directly, we constructed 24 binary label masks per atlas pair (one per structure) and optimized
220 alignment using the mean squares similarity metric with the SyN transform⁵⁰.

221 To generate the point sets for velocity field optimization, we sampled both boundary (contour)
222 and interior (region) points from the P56 labels and propagated them to each developmental
223 stage using the learned pairwise transforms. Contours were sampled at 10% of available points

²²⁴ and regions at 1%, yielding 173,303 total points per atlas ($N_{contour} = 98,151$; $N_{region} = 75,152$).
²²⁵ Boundary points were assigned double weight during optimization to emphasize anatomical
²²⁶ boundary correspondence.

²²⁷ **2.2.2 Velocity field optimization**

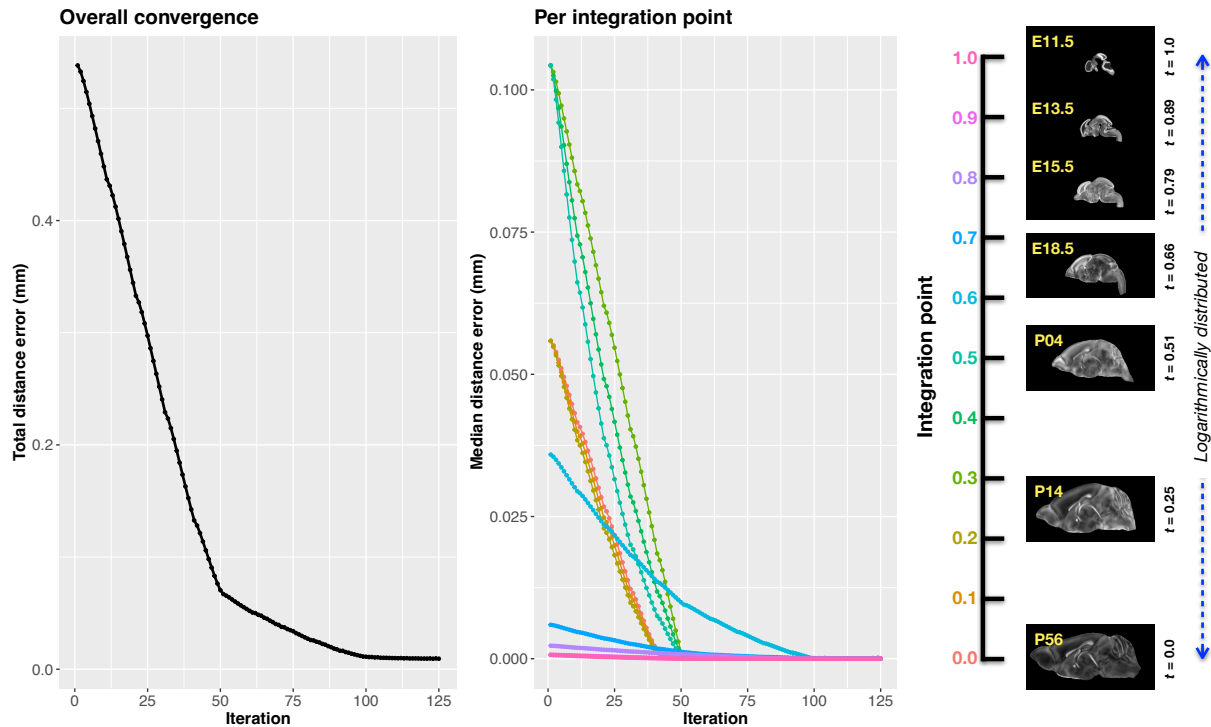


Figure 4: Convergence of velocity field optimization across the DevCCF developmental trajectory. Integration points (color-coded) are distributed along the log-scaled time axis.

²²⁸ The velocity field was optimized using the seven corresponding point sets and their associated
²²⁹ weights. The field geometry was defined at [256, 182, 360] with 11 integration points at 50
²³⁰ μm resolution, yielding a compressed velocity model of ~ 2 GB. This resolution balanced
²³¹ accuracy and computational tractability while remaining portable. All data and code are
²³² publicly available in the accompanying GitHub repository.
²³³ To normalize temporal spacing, we assigned scalar values in $[0, 1]$ to each template. Given the
²³⁴ nonlinear spacing in postnatal development, we applied a logarithmic transform to the raw
²³⁵ time values prior to normalization. P56 was assigned a span of 28 postnatal days to reflect

²³⁶ known developmental dynamics, which improved the temporal distribution of integration
²³⁷ points (Figure 4, right panel).

²³⁸ Optimization was run for a maximum of 200 iterations using a 2020 iMac (3.6 GHz 10-Core
²³⁹ Intel Core i9, 64 GB RAM), with each iteration taking \sim 6 minutes. During each iteration,
²⁴⁰ the velocity field was updated across all 11 integration points by computing regularized
²⁴¹ displacement fields between warped point sets at adjacent time slices. Updates were applied
²⁴² using a step size of $\delta = 0.2$. Convergence was assessed via average displacement error across
²⁴³ all points, with final convergence achieved after \sim 125 iterations (Figure 4, left panel). Median
²⁴⁴ errors across integration points also trended toward zero, albeit at varying rates.

²⁴⁵ **2.2.3 The velocity flow transformation model**

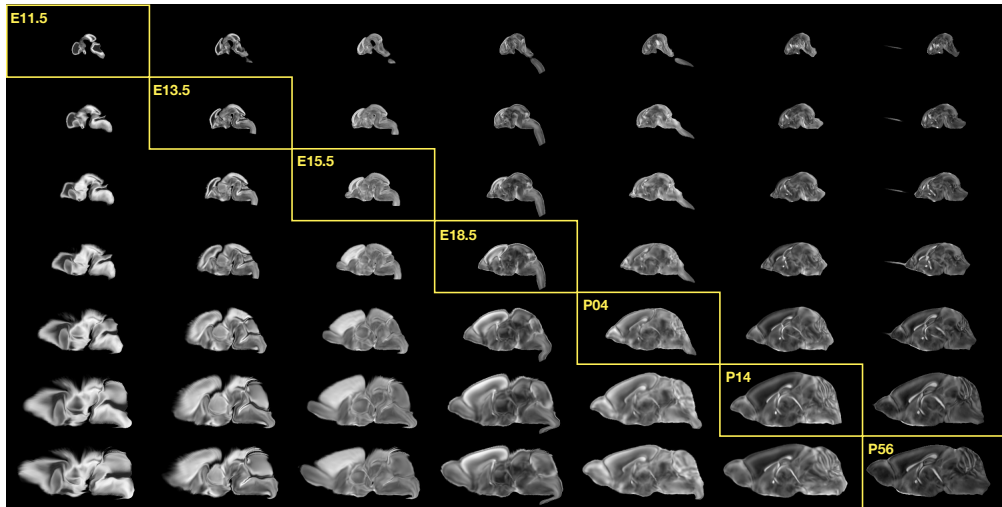


Figure 5: Mid-sagittal visualization of DevCCF templates warped to every other time point. Each row is a reference space; each column is a warped input. Diagonal entries show original templates.

²⁴⁶ Once optimized, the velocity field enables the computation of diffeomorphic transformations
²⁴⁷ between any pair of continuous time points within the DevCCF developmental range. Figure 5
²⁴⁸ illustrates cross-warping between all DevCCF stages using the learned velocity flow model. In
²⁴⁹ addition to facilitating flexible alignment between existing templates, the model also supports
²⁵⁰ the synthesis of virtual templates at intermediate, unsampled developmental stages.

²⁵¹ As shown in Figure 6, we demonstrate the creation of virtual age templates (e.g., P10.3 and

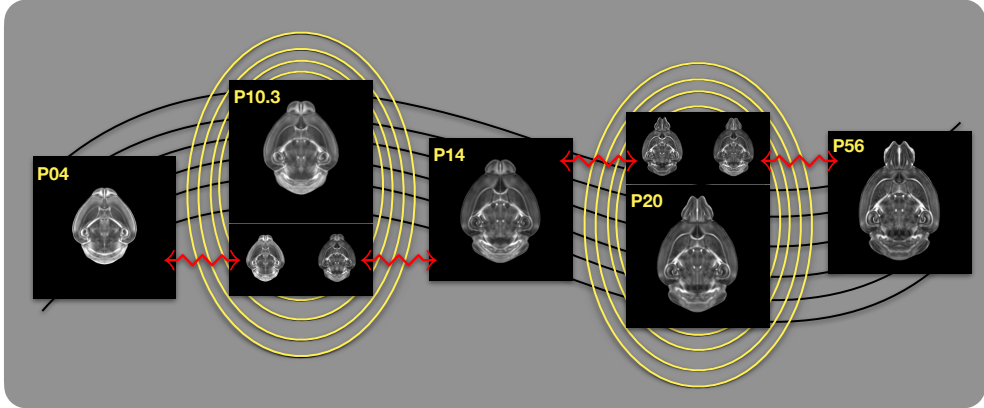


Figure 6: Example of generating “virtual” DevCCF templates at intermediate time points (e.g., P10.3, P20) by warping adjacent stages to a shared time and averaging using ANTsX.

252 P20) by warping adjacent developmental atlases to a target timepoint and constructing an
253 averaged representation using ANTsX’s template-building functionality.

254 All usage examples, scripts, and supporting data are publicly available in the associated
255 codebase.

256 2.3 Automated structural parcellations of the mouse brain

257 Brain parcellation strategies for the mouse brain are pivotal for understanding the complex
258 organization and function of murine nervous system⁸¹. By dividing the brain into distinct
259 regions based on anatomical, physiological, or functional characteristics, researchers can
260 investigate specific areas in isolation and identify their roles in various behaviors and processes.
261 For example, such parcellation schemes can help elucidate the spatial distribution of gene
262 expression patterns⁸² as well as identify functional regions involved in specific cognitive
263 tasks⁸³.

264 Although deep learning techniques have been used to develop useful parcellation tools for
265 human brain research (e.g., SynthSeg⁸⁴, ANTsXNet⁴⁴), analogous development for the mouse
266 brain is limited. In addition, mouse data is often characterized by unique imaging issues
267 such as extreme anisotropic sampling which are often in sharp contrast to the high resolution
268 template-based resources available within the community, e.g., AllenCCFv3 and DevCCF. We

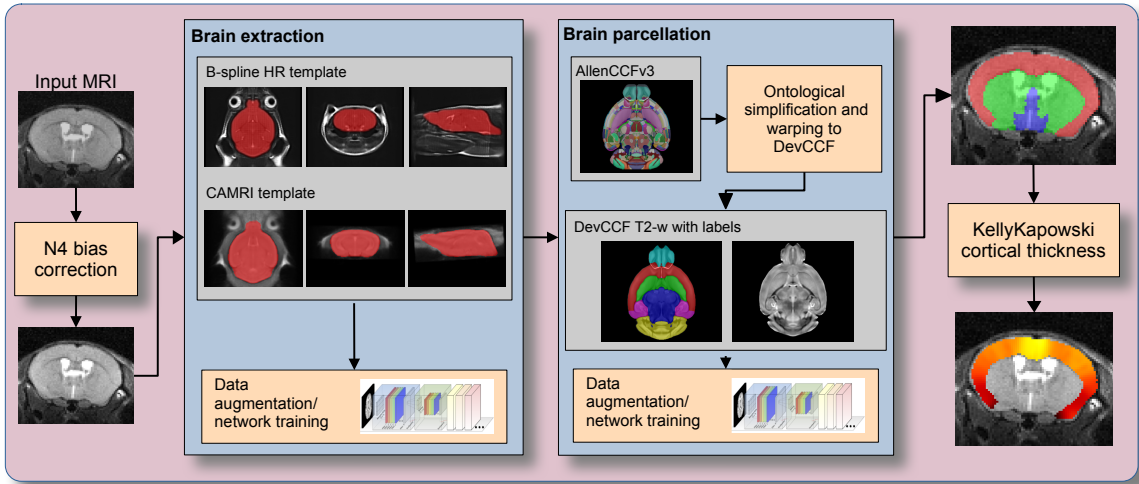


Figure 7: The mouse brain cortical parcellation pipeline integrating two deep learning components for brain extraction and brain parcellation prior to estimating cortical labels. Both deep learning networks rely heavily on aggressive data augmentation on templates built from open data and provide an outline for further refinement and creating alternative parcellations for tailored research objectives. Possible applications include voxelwise cortical thickness measurements.

²⁶⁹ demonstrate how one can use the ANTsX tools to develop a complete mouse brain structural
²⁷⁰ morphology pipeline as illustrated in Figure 7 and detailed below.

²⁷¹ 2.3.1 Few-shot mouse brain extraction network

²⁷² In order to create a generalized mouse brain extraction network, we built whole-head templates
²⁷³ from two publicly available datasets. The Center for Animal MRI (CAMRI) dataset⁶⁷ from
²⁷⁴ the University of North Carolina at Chapel Hill consists of 16 T2-w MRI volumes of voxel
²⁷⁵ resolution $0.16 \times 0.16 \times 0.16 mm^3$. The second high-resolution dataset⁶⁸ comprises 88 specimens
²⁷⁶ each with three spatially aligned canonical views with in-plane resolution of $0.08 \times 0.08 mm^2$
²⁷⁷ with a slice thickness of $0.5 mm$. These three orthogonal views were used to reconstruct
²⁷⁸ a single high-resolution volume per subject using a B-spline fitting algorithm available in
²⁷⁹ ANTsX⁸⁵.

²⁸⁰ From these two datasets, two ANTsX templates⁵⁸ were generated. Bias field simulation,
²⁸¹ intensity histogram warping, noise simulation, random translation and warping, and random
²⁸² anisotropic resampling in the three canonical directions were used for data augmentation

283 in training an initial T2-w brain extraction network. This network was posted and the
284 corresponding functionality was immediately made available within ANTsXNet, similar to
285 our previous contributions to the community.

286 User interest led to a GitHub inquiry regarding possible study-specific improvements (<https://github.com/ANTsX/ANTsPyNet/issues/133>). This interaction led to the offering of a
287 user-made third template and extracted brain mask generated from T2-w ex-vivo data with
288 isotropic spacing of 0.08 mm in each voxel dimension. This third template, in conjunction
289 with the other two, were used with the same aggressive data augmentation to refine the
290 network weights which were subsequently posted and made available through ANTsPyNet
291 using the function `antspynet.mouse_brain_extraction(...)`.

293 2.3.2 Single-shot mouse brain parcellation network

294 AllenCCFv3 and its hierarchical ontological labeling, along with the DevCCF, provides the
295 necessary data for developing a tailored structural parcellation network for multi-modal
296 imaging. The `allensdk` Python library permits the creation of any gross parcellation based
297 on the AllenCCFv3 ontology. Specifically, using `allensdk` we coalesced the labels to the
298 following six major structures: cerebral cortex, cerebral nuclei, brain stem, cerebellum, main
299 olfactory bulb, and hippocampal formation. This labeling was mapped to the P56 component
300 of the DevCCF for use with the T2-w template component.

301 The T2-w P56 DevCCF and labelings, in conjunction with the data augmentation
302 described previously for brain extraction, were used to train the proposed brain
303 parcellation network. This is available in ANTsXNet (e.g. in ANTsPyNet using
304 `antspynet.mouse_brain_parcellation(...)`). Note that other brain parcellation net-
305 works have also been trained using alternative regions and parcellation schemes and are
306 available in the same ANTsXNet functionality. One usage note is that the data augmentation
307 used to train the network permits a learned interpolation in 0.08 mm isotropic space. Since
308 the training data is isotropic and data augmentation includes downsampling in the canonical
309 directions, each of the two networks learns mouse brain-specific interpolation such that
310 one can perform prediction on thick-sliced images, as, for example, in these evaluation

311 data, and return isotropic probability and thickness maps (a choice available to the user).
312 This permits robust cortical thickness estimation even in the case of anisotropic data (see
313 `antspynet.mouse_cortical_thickness(...)`).

314 **2.3.3 Evaluation**

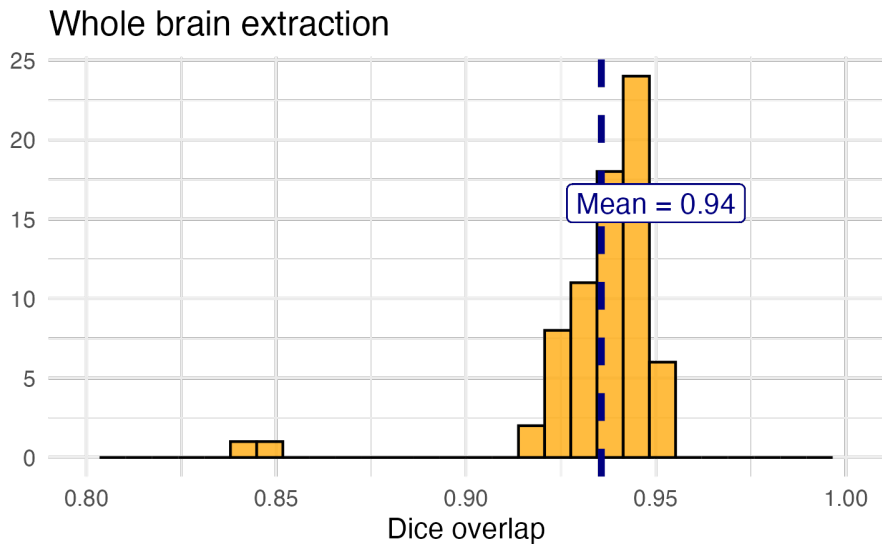
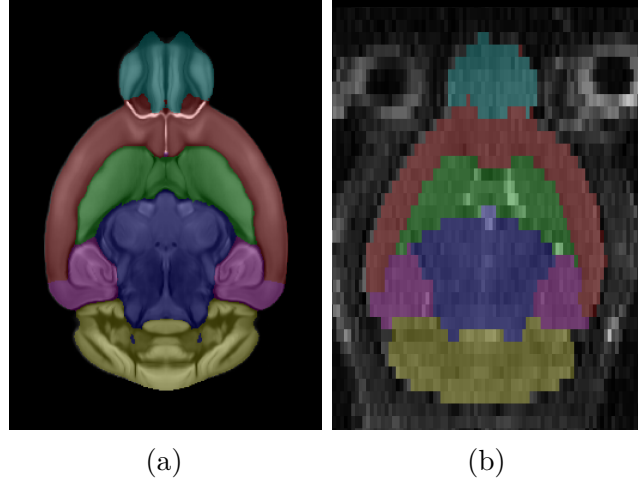


Figure 8: Evaluation of the ANTsX mouse brain extraction on an independent, publicly available dataset consisting of 12 specimens \times 7 time points = 84 total images. Dice overlap comparisons with the user-generated brain masks provide good agreement with the automated results from the brain extraction network.

315 For evaluation, we used an additional publicly available dataset⁶⁹ that is completely indepen-
316 dent from the data used in training the brain extraction and parcellation networks. Data
317 includes 12 specimens each imaged at seven time points (Day 0, Day 3, Week 1, Week 4,
318 Week 8, Week 20) with in-house-generated brain masks for a total of 84 images. Spacing is
319 anistropic with an in-plane resolution of $0.1 \times 0.1 mm^2$ and a slice thickness of $0.5 mm$.

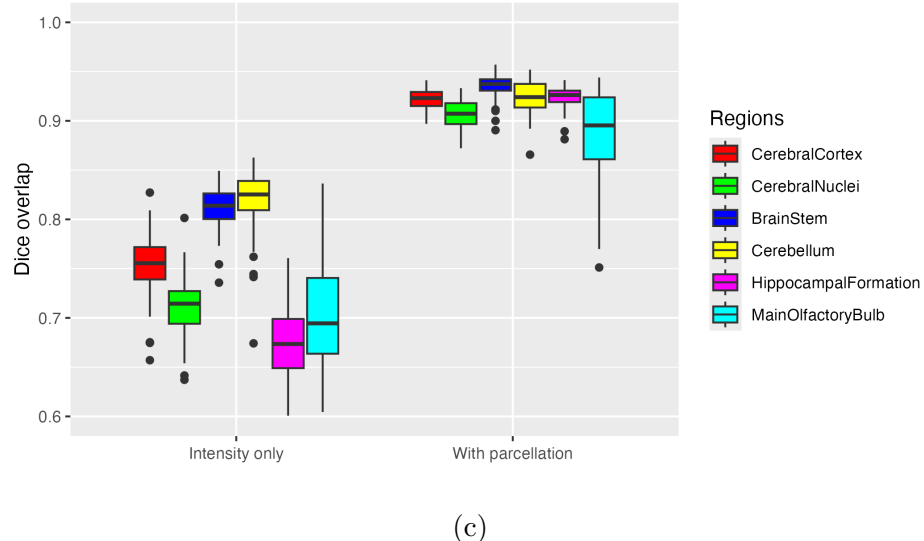
320 Figure 8 summarizes the whole brain overlap between the provided segmentations for all
321 84 images and the results of applying the proposed network. Also, since mapping to the
322 AllenCCFv3 atlas is crucial for many mouse studies, we demonstrate the utility of the second
323 network by leveraging the labeled regions to perform anatomically-explicit alignment using
324 ANTsX multi-component registration instead of intensity-only registration. For these data,



(a)

(b)

Normalization to AllenCCFv3



(c)

Figure 9: Evaluation of the ANTsX mouse brain parcellation on the same dataset. (a) T2-w DevCCF P56 with the described parcellation consisting of the cerebral cortex, nuclei, brain stem, cerebellum, main olfactory bulb, and hippocampal formation. (b) Sample subject (NR5 Day 0) with the proposed deep learning-based segmentation. (c) Dice overlap for comparing the regional alignments between registration using intensity information only and using intensity with the given parcellation scheme.

³²⁵ the whole brain extraction demonstrates excellent performance across the large age range.
³²⁶ And although the intensity-only image registration provides adequate alignment, intensity
³²⁷ with the regional parcellations significantly improves those measures.

328 **3 Discussion**

329 The diverse mouse brain cell type profiles gathered through BICCN and associated efforts
330 provide a rich multi-modal resource to the research community. However, despite significant
331 progress, optimal leveraging of these valuable resources remains an ongoing challenge. A
332 central component to data integration is accurately mapping novel cell type data into
333 common coordinate frameworks (CCFs) for subsequent processing and analysis. To meet
334 these needs, tools for mapping mouse brain data must be both broadly accessible and
335 capable of addressing challenges unique to each modality. In this work, we described modular
336 ANTsX-based pipelines developed to support three distinct BICCN efforts encompassing
337 spatial transcriptomic, morphological, and developmental data. We demonstrated how a
338 flexible image analysis toolkit like ANTsX can be tailored to address specific modality-driven
339 constraints by leveraging reusable, validated components.

340 The MERFISH mapping pipeline illustrates how ANTsX tools can be adapted to accommodate
341 high-resolution spatial transcriptomic data. While the general mapping strategy is applicable
342 to other sectioned histological data, the pipeline includes specific adjustments for known
343 anatomical and imaging artifacts present in MERFISH datasets. As such, this example
344 demonstrates how general-purpose tools can be customized to meet the requirements of highly
345 specialized data types.

346 The fMOST mapping pipeline was developed with the intention of broader applicability.
347 Built primarily from existing ANTsX preprocessing and registration modules, this pipeline
348 introduces an fMOST-specific intermediate atlas to facilitate consistent mappings to the
349 AllenCCFv3. The use of a canonical fMOST atlas reduces the need for repeated manual
350 alignment across new datasets, and the resulting transformations can be directly applied to
351 associated single-neuron reconstructions. This supports integrative morphological analysis
352 across specimens using a common coordinate system.

353 For developmental data, we introduced a velocity field-based model for continuous interpo-
354 lation between discrete DevCCF timepoints. Although the DevCCF substantially expands
355 coverage of developmental stages relative to prior atlases, temporal gaps remain. The velocity

356 model enables spatio-temporal transformations within the full developmental interval and
357 supports the generation of virtual templates at unsampled ages. This functionality is built
358 using ANTsX components for velocity field optimization and integration, and offers a novel
359 mechanism for interpolating across the non-linear developmental trajectory of the mouse brain.
360 Such interpolation has potential utility for both anatomical harmonization and longitudinal
361 analyses.

362 We also introduced a template-based deep learning pipeline for mouse brain extraction and
363 parcellation using aggressive data augmentation. This approach is designed to reduce the
364 reliance on large annotated training datasets, which remain limited in the mouse imaging
365 domain. Evaluation on independent data demonstrates promising generalization, though
366 further refinement will be necessary. As with our human-based ANTsX pipelines, failure
367 cases can be manually corrected and recycled into future training cycles. Community
368 contributions are welcomed and encouraged, providing a pathway for continuous improvement
369 and adaptation to new datasets.

370 The ANTsX ecosystem offers a powerful foundation for constructing scalable, reproducible
371 pipelines for mouse brain data analysis. Its modular design and multi-platform support enable
372 researchers to develop customized workflows without extensive new software development.

373 The widespread use of ANTsX components across the neuroimaging community attests to its
374 utility and reliability. As a continuation of the BICCN program, ANTsX is well positioned to
375 support the goals of the BRAIN Initiative Cell Atlas Network (BICAN) and future efforts to
376 extend these mapping strategies to the human brain.

³⁷⁷ **4 Methods**

³⁷⁸ The following methods are all available as part of the ANTsX ecosystem with analogous
³⁷⁹ elements existing in both ANTsR (ANTs in R) and ANTsPy (ANTs in Python), underpinned by
³⁸⁰ a shared ANTs/ITK C++ core. Most development for the work described was performed using
³⁸¹ ANTsPy. For equivalent functionality in ANTsR, we refer the reader to the comprehensive
³⁸² ANTsX tutorial: <https://tinyurl.com/antsxtutorial>.

³⁸³ **4.1 General ANTsX utilities**

³⁸⁴ Although focused on distinct data types, the three pipelines presented in this work share
³⁸⁵ common components that address general challenges in mapping mouse brain data. These
³⁸⁶ include correcting image intensity artifacts, denoising, spatial registration, template generation,
³⁸⁷ and visualization. Table 1 provides a concise summary of the relevant ANTsX functionality.

³⁸⁸ **Preprocessing: bias field correction and denoising.** Standard preprocessing steps in
³⁸⁹ mouse brain imaging include correcting for spatial intensity inhomogeneities and reducing
³⁹⁰ image noise, both of which can impact registration accuracy and downstream analysis. ANTsX
³⁹¹ provides implementations of widely used methods for these tasks. The N4 bias field correction
³⁹² algorithm⁵¹, originally developed in ANTs and contributed to ITK, mitigates artifactual, low-
³⁹³ frequency intensity variation and is accessible via `ants.n4_bias_field_correction(...)`.
³⁹⁴ Patch-based denoising⁶⁰ has been implemented as `ants.denoise_image(...)`.

³⁹⁵ **Image registration.** ANTsX includes a robust and flexible framework for pairwise
³⁹⁶ and groupwise image registration⁸⁶. At its core is the SyN algorithm⁵⁰, a symmetric
³⁹⁷ diffeomorphic model with optional B-spline regularization⁶⁶. In ANTsPy, registration
³⁹⁸ is performed via `ants.registration(...)` using preconfigured parameter sets (e.g.,
³⁹⁹ `antsRegistrationSyNQuick[s]`, `antsRegistrationSyN[s]`) suitable for different imaging
⁴⁰⁰ modalities and levels of computational demand. Resulting transformations can be applied to
⁴⁰¹ new images with `ants.apply_transforms(...)`.

⁴⁰² **Template generation.** ANTsX supports population-based template generation through
⁴⁰³ iterative pairwise registration to an evolving estimate of the mean shape and intensity

Table 1: Sampling of ANTsX functionality

<i>ANTsPy: Preprocessing</i>	
bias field correction	<code>n4_bias_field_correction(...)</code>
image denoising	<code>denoise_image(...)</code>
<i>ANTsPy: Registration</i>	
image registration	<code>registration(...)</code>
image transformation	<code>apply_transforms(...)</code>
template generation	<code>build_template(...)</code>
landmark registration	<code>fit_transform_to_paired_points(...)</code>
time-varying landmark reg.	<code>fit_time_varying_transform_to_point_sets(...)</code>
integrate velocity field	<code>integrate_velocity_field(...)</code>
invert displacement field	<code>invert_displacement_field(...)</code>
<i>ANTsPy: Segmentation</i>	
MRF-based segmentation	<code>atropos(...)</code>
Joint label fusion	<code>joint_label_fusion(...)</code>
diffeomorphic thickness	<code>kelly_kapowski(...)</code>
<i>ANTsPy: Miscellaneous</i>	
Regional intensity statistics	<code>label_stats(...)</code>
Regional shape measures	<code>label_geometry_measures(...)</code>
B-spline approximation	<code>fit_bspline_object_to_scattered_data(...)</code>
Visualize images and overlays	<code>plot(...)</code>
<i>ANTsPyNet: Mouse-specific</i>	
brain extraction	<code>mouse_brain_extraction(...modality="t2"...)</code>
brain parcellation	<code>mouse_brain_parcellation(...)</code>
cortical thickness	<code>mouse_cortical_thickness(...)</code>
super resolution	<code>mouse_histology_super_resolution(...)</code>

ANTsX provides state-of-the-art functionality for processing biomedical image data. Such tools, including deep learning networks, support a variety of mapping-related tasks. A more comprehensive listing of ANTsX tools with self-contained R and Python examples is provided as a gist page on GitHub (<https://tinyurl.com/antsxtutorial>).

404 reference space across subjects⁵⁸. This functionality was used in generating the DevCCF
405 templates¹⁶. The procedure, implemented as `ants.build_template(...)`, produces average
406 images in both shape and intensity by aligning all inputs to a common evolving template.

407 **Visualization.** To support visual inspection and quality control, ANTsPy provides flexible
408 image visualization with `ants.plot(...)`. This function enables multi-slice and multi-
409 orientation rendering with optional overlays and label maps.

410 4.2 Mapping fMOST data to AllenCCFv3

411 **Preprocessing.** Mapping fMOST data into the AllenCCFv3 presents unique challenges due
412 to its native ultra-high resolution and imaging artifacts common to the fMOST modality.
413 Each fMOST image can exceed a terabyte in size, with spatial resolutions far exceeding
414 those of the AllenCCFv3 ($25\ \mu m$ isotropic). To reduce computational burden and prevent
415 resolution mismatch, each fMOST image is downsampled using cubic B-spline interpolation
416 via `ants.resample_image(...)` to match the template resolution.

417 Stripe artifacts (i.e., periodic intensity distortions caused by nonuniform sectioning or illumina-
418 nation) are common in fMOST and can mislead deformable registration algorithms. These
419 were removed using a custom 3D notch filter (`remove_stripe_artifact(...)`) implemented
420 in the `CCFAlignmentToolkit` using SciPy frequency domain filtering. The filter targets
421 dominant stripe frequencies along a user-specified axis in the Fourier domain. In addition,
422 intensity inhomogeneity across sections, often arising from variable staining or illumination,
423 was corrected using N4 bias field correction.

424 **Template-based spatial normalization.** To facilitate reproducible mapping, we first
425 constructed a contralaterally symmetric average template from 30 fMOST brains and their
426 mirrored counterparts using ANTsX template-building tools. Because the AllenCCFv3 and
427 fMOST data differ substantially in both intensity contrast and morphology, direct deformable
428 registration between individual fMOST brains and the AllenCCFv3 was insufficiently robust.
429 Instead, we performed a one-time expert-guided label-driven registration between the average
430 fMOST template and AllenCCFv3. This involved sequential alignment of seven manually

431 selected anatomical regions: 1) brain mask/ventricles, 2) caudate/putamen, 3) fimbria, 4)
432 posterior choroid plexus, 5) optic chiasm, 6) anterior choroid plexus, and 7) habenular
433 commissure which were prioritized to enable coarse-to-fine correction of shape differences.
434 Once established, this fMOST-template-to-AllenCCFv3 transform was reused for all subse-
435 quent specimens. Each new fMOST brain was then registered to the average fMOST template
436 using intensity-based registration, followed by concatenation of transforms to produce the
437 final mapping into AllenCCFv3 space.

438 **Mapping neuron projections.** A key advantage of fMOST imaging is its ability to
439 support single neuron projection reconstruction across the entire brain⁷⁷. Because these
440 reconstructions are stored as 3D point sets aligned to the original fMOST volume, we applied
441 the same composite transform used for image alignment to the point data using ANTsX
442 functionality. This enables seamless integration of cellular morphology data into AllenCCFv3
443 space, facilitating comparative analyses across specimens.

444 4.3 Mapping MERFISH data to AllenCCFv3

445 **Preprocessing.** MERFISH data are acquired as a series of 2D tissue sections, each comprising
446 spatially localized gene expression measurements at subcellular resolution. To enable 3D
447 mapping to the AllenCCFv3, we first constructed anatomical reference images by aggregating
448 the number of detected transcripts per voxel across all probes within each section. These 2D
449 projections were resampled to a resolution of $10 \mu m \times 10 \mu m$ to match the in-plane resolution
450 of the AllenCCFv3.

451 Sections were coarsely aligned using manually annotated dorsal and ventral midline points,
452 allowing initial volumetric reconstruction. However, anatomical fidelity remained limited by
453 variation in section orientation, spacing, and tissue loss. To further constrain alignment and
454 enable deformable registration, we derived region-level anatomical labels directly from the
455 gene expression data.

456 **Label creation.** We assigned each detected cell to one of 15 coarse anatomical regions (e.g.,
457 hippocampus, cortex, striatum—using transcriptomic similarity to scRNA) seq reference

458 data. These assignments were aggregated across spatial grids to produce probabilistic label
459 maps for each section. To ensure full regional coverage, morphological dilation was applied to
460 fill gaps between sparsely distributed cells. Finer-resolution structures (e.g., cortical layers,
461 habenula) were similarly labeled using marker gene enrichment and spatial constraints. This
462 dual-level labeling (i.e., coarse and fine) allowed us to construct a robust anatomical scaffold
463 in the MERFISH coordinate system that could be matched to AllenCCFv3 annotations.

464 **Section matching via global alignment.** A major challenge was compensating for oblique
465 cutting angles and non-uniform section thickness, which distort the anatomical shape and
466 spacing of the reconstructed volume. Rather than directly warping the MERFISH data into
467 atlas space, we globally aligned the AllenCCFv3 to the MERFISH coordinate system. This
468 was done via an affine transformation followed by resampling of AllenCCFv3 sections to match
469 the number and orientation of MERFISH sections. This approach minimizes interpolation
470 artifacts in the MERFISH data and facilitates one-to-one section matching.

471 **Landmark-driven deformable alignment.** We used a 2.5D approach for fine alignment of
472 individual sections. In each MERFISH slice, deformable registration was driven by sequential
473 alignment of anatomical landmarks between the label maps derived from MERFISH and
474 AllenCCFv3. A total of nine regions—including isocortical layers 2/3, 5, and 6, the striatum,
475 hippocampus, thalamus, and medial/lateral habenula—were registered in an empirically
476 determined order. After each round, anatomical alignment was visually assessed by an expert,
477 and the next structure was selected to maximize improvement in the remaining misaligned
478 regions.

479 The final transform for each section combined the global affine alignment and the per-structure
480 deformable registrations. These were concatenated to generate a 3D mapping from the original
481 MERFISH space to the AllenCCFv3 coordinate system. Once established, the composite
482 mapping enables direct transfer of gene-level and cell-type data from MERFISH into atlas
483 space, allowing integration with other imaging and annotation datasets.

484 4.4 DevCCF velocity flow transformation model

485 The Developmental Common Coordinate Framework (DevCCF)¹⁶ provides a discrete set of
486 age-specific templates that temporally sample the developmental trajectory. To model this
487 biological progression more continuously, we introduce a velocity flow-based paradigm for
488 inferring diffeomorphic transformations between developmental stages. This enables anatom-
489 ically plausible estimation of intermediate templates or mappings at arbitrary timepoints
490 between the E11.5 and P56 endpoints of the DevCCF. Our approach builds on established
491 insights from time-varying diffeomorphic registration⁶⁵, where a velocity field governs the
492 smooth deformation of anatomical structures over time. Importantly, the framework is
493 extensible and can naturally accommodate additional timepoints for the potential expansion
494 of the DevCCF.

495 **Point sampling and region correspondence.** We first coalesced the anatomical labels
496 across the seven DevCCF templates (E11.5, E13.5, E15.5, E18.5, P4, P14, P56) into 26
497 common structures that could be consistently identified across development. These include
498 major brain regions such as the cortex, cerebellum, hippocampus, midbrain, and ventricles.
499 For each successive pair of templates, we performed multi-label deformable registration
500 using ANTsX to generate forward and inverse transforms between anatomical label volumes.
501 From the P56 space, we randomly sampled approximately 1e6 points within and along the
502 boundaries of each labeled region and propagated them through each pairwise mapping step
503 (e.g., P56 → P14, P14 → P4, ..., E13.5 → E11.5). This procedure created time-indexed
504 point sets tracing the spatial evolution of each region.

505 **Velocity field fitting.** Using these point sets, we fit a continuous velocity field over
506 developmental time using a generalized B-spline scattered data approximation method⁸⁵.
507 The field was parameterized over a log-scaled time axis to ensure finer temporal resolution
508 during early embryonic stages, where morphological changes are most rapid. Optimization
509 proceeded for approximately 125 iterations, minimizing the average Euclidean norm between
510 transformed points at each step. Ten integration points were used to ensure numerical
511 stability. The result is a smooth, differentiable vector field that defines a diffeomorphic
512 transform between any two timepoints within the template range.

513 **Applications and availability.** This velocity model can be used to estimate spatial transfor-
514 mations between any pair of developmental stages—even those for which no empirical template
515 exists—allowing researchers to create interpolated atlases, align new datasets, or measure con-
516 tinuous structural changes. It also enables developmental alignment of multi-modal data (e.g.,
517 MRI to LSFM) by acting as a unifying spatiotemporal scaffold. The underlying components
518 for velocity field fitting and integration are implemented in ITK, and the complete workflow
519 is accessible in both ANTsPy (`ants.fit_time_varying_transform_to_point_sets(...)`)
520 and ANTsR. In addition the availability of the DevCCF use case, self-contained examples
521 and usage tutorials are provided in our public codebase.

522 4.5 Automated brain extraction and parcellation with ANTsXNet

523 To support template-based deep learning approaches for structural brain extraction and par-
524 cellation, we implemented dedicated pipelines using the ANTsXNet framework. ANTsXNet
525 comprises open-source deep learning libraries in both Python (ANTsPyNet) and R (ANTsR-
526 Net) that interface with the broader ANTsX ecosystem and are built on TensorFlow/Keras.
527 Our mouse brain pipelines mirror existing ANTsXNet tools for human imaging but are
528 adapted for species-specific anatomical variation, lower SNR, and heterogeneous acquisition
529 protocols.

530 4.5.1 Deep learning training setup

531 All networks were implemented in ANTsPyNet using standard 3D U-net architectures⁸⁷
532 previously employed in previously published work⁴⁴. Training was performed on an NVIDIA
533 DGX system (4 × Tesla V100 GPUs, 256 GB RAM). Model weights and preprocessing
534 routines are shared across ANTsPyNet and ANTsRNet to ensure reproducibility and lan-
535 guage portability. For both published and unpublished trained networks available through
536 ANTsXNet, all training scripts and data augmentation generators are publicly available at
537 <https://github.com/ntustison/ANTsXNetTraining>.

538 **Data augmentation.** Robust data augmentation was critical to generalization across

539 scanners, contrast types, and resolutions. We applied both intensity- and shape-based
540 augmentation strategies:

541 • *Intensity augmentations:*

- 542 – Gaussian, Poisson, and salt-and-pepper noise:
543 `ants.add_noise_to_image(...)`
- 544 – Simulated intensity inhomogeneity via bias field modeling⁵¹:
545 `antspynet.simulate_bias_field(...)`
- 546 – Histogram warping to simulate contrast variation⁸⁸:
547 `antspynet.histogram_warp_image_intensities(...)`

548 • *Shape augmentations:*

- 549 – Random nonlinear deformations and affine transforms:
550 `antspynet.randomly_transform_image_data(...)`
- 551 – Anisotropic resampling across axial, sagittal, and coronal planes:
552 `ants.resample_image(...)`

553 **4.5.2 Brain extraction**

554 We originally trained a mouse-specific brain extraction model on two manually masked
555 T2-weighted templates, generated from public datasets^{67,68}. One of the templates was
556 constructed from orthogonal 2D acquisitions using B-spline-based volumetric synthesis
557 via `ants.fit_bspline_object_to_scattered_data(...)`. Normalized gradient magnitude
558 was used as a weighting function to emphasize boundaries during reconstruction⁸⁵.

559 This training strategy provides strong spatial priors despite limited data by leveraging
560 high-quality template images and aggressive augmentation to mimic population variability.
561 During the development of this work, the network was further refined through community
562 engagement. A user from a U.S.-based research institute applied the publicly available (but
563 then unpublished) brain extraction tool to their own mouse MRI dataset. Based on feedback
564 and iterative collaboration with the ANTsX team, the model was retrained and improved to

565 better generalize to additional imaging contexts. This reflects our broader commitment to
566 community-driven development and responsiveness to user needs across diverse mouse brain
567 imaging scenarios.

568 The final trained network is available via ANTsXNet through the function
569 `antspynet.mouse_brain_extraction(...)`. Additionally, both template/mask pairs are
570 accessible via ANTsXNet. For example, one such image pair is available via:

- Template:

```
572     antspynet.get_antsxnet_data("bsplineT2MouseTemplate")
```

- Brain mask:

```
574     antspynet.get_antsxnet_data("bsplineT2MouseTemplateBrainMask")
```

575 4.5.3 Brain parcellation

576 For brain parcellation, we trained a 3D U-net model using the DevCCF P56 T2-weighted
577 template and anatomical segmentations derived from AllenCCFv3. This template-based
578 training strategy enables the model to produce accurate, multi-region parcellations without
579 requiring large-scale annotated subject data.

580 To normalize intensity across specimens, input images were preprocessed using rank-based
581 intensity normalization (`ants.rank_intensity(...)`). Spatial harmonization was achieved
582 through affine and deformable alignment of each extracted brain to the P56 template prior
583 to inference. In addition to the normalized image input, the network also receives prior
584 probability maps derived from the atlas segmentations, providing additional spatial context.

585 This general parcellation deep learning framework has also been applied in collaboration
586 with other groups pursuing related but distinct projects. In one case, a model variant
587 was adapted for T2-weighted MRI using an alternative anatomical labeling scheme; in
588 another, a separate model was developed for serial two-photon tomography (STPT) with
589 a different parcellation set. All three models are accessible through a shared interface
590 in ANTsXNet: `antspynet.mouse_brain_parcellation(...)`. Ongoing work is further
591 extending this approach to embryonic mouse brain data. These independent efforts reflect

592 broader community interest in adaptable parcellation tools and reinforce the utility of
593 ANTsXNet as a platform for reproducible, extensible deep learning workflows.

594 **4.5.4 Evaluation and reuse**

595 To assess model generalizability, both the brain extraction and parcellation networks were
596 evaluated on an independent longitudinal dataset comprising multiple imaging sessions
597 with varied acquisition parameters⁶⁹. Although each label or imaging modality required
598 retraining, the process was streamlined by the reusable ANTsX infrastructure enabled by
599 rapid adaptation with minimal overhead. These results illustrate the practical benefits of a
600 template-based, low-shot strategy and modular deep learning framework. All trained models,
601 associated training scripts, and supporting resources are openly available and designed for
602 straightforward integration into ANTsX workflows.

603 **Data availability**

604 All data and software used in this work are publicly available. The DevCCF atlas is
605 available at <https://kimlab.io/brain-map/DevCCF/>. ANTsPy, ANTsR, ANTsPyNet, and
606 ANTsRNet are available through GitHub at the ANTsX Ecosystem (<https://github.com/ANTsX>). Training scripts for all deep learning functionality in ANTsXNet can also be found on
607 GitHub (<https://github.com/ntustison/ANTsXNetTraining>). A GitHub repository specifically
608 pertaining to the AllenCCFv3 mapping is available at <https://github.com/dontminchenit/>
609 [CCFAAlignmentToolkit](#). For the other two contributions contained in this work, the longitudinal
610 DevCCF mapping and mouse cortical thickness pipeline, we refer the interested reader to
611 <https://github.com/ntustison/ANTsXMouseBrainMapping>.

⁶¹³ **Acknowledgments**

⁶¹⁴ Support for the research reported in this work includes funding from the National Institute
⁶¹⁵ of Biomedical Imaging and Bioengineering (R01-EB031722) and National Institute of Mental
⁶¹⁶ Health (RF1-MH124605 and U24-MH114827).

⁶¹⁷ We also acknowledge the data contribution of Dr. Adam Raikes (GitHub @araikes) of the
⁶¹⁸ Center for Innovation in Brain Science at the University of Arizona for refining the weights
⁶¹⁹ of the mouse brain extraction network.

620 **Author contributions**

621 N.T., M.C., and J.G. wrote the main manuscript text and figures. M.C., M.K., R.D., S.S.,
622 Q.W., L.G., J.D., C.G., and J.G. developed the Allen registration pipelines. N.T. and F.K.
623 developed the time-varying velocity transformation model for the DevCCF. N.T. and M.T.
624 developed the brain parcellation and cortical thickness methodology. All authors reviewed
625 the manuscript.

626 **References**

- 627 1. Keller, P. J. & Ahrens, M. B. Visualizing whole-brain activity and development at the
single-cell level using light-sheet microscopy. *Neuron* **85**, 462–83 (2015).
- 628 2. La Manno, G. *et al.* Molecular architecture of the developing mouse brain. *Nature*
596, 92–96 (2021).
- 629 3. Wen, L. *et al.* Single-cell technologies: From research to application. *Innovation
(Camb)* **3**, 100342 (2022).
- 630 4. Oh, S. W. *et al.* A mesoscale connectome of the mouse brain. *Nature* **508**, 207–14
(2014).
- 631 5. Gong, H. *et al.* Continuously tracing brain-wide long-distance axonal projections in
mice at a one-micron voxel resolution. *Neuroimage* **74**, 87–98 (2013).
- 632 6. Li, A. *et al.* Micro-optical sectioning tomography to obtain a high-resolution atlas of
the mouse brain. *Science* **330**, 1404–8 (2010).
- 633 7. Ueda, H. R. *et al.* Tissue clearing and its applications in neuroscience. *Nat Rev
Neurosci* **21**, 61–79 (2020).
- 634 8. Ståhl, P. L. *et al.* Visualization and analysis of gene expression in tissue sections by
spatial transcriptomics. *Science* **353**, 78–82 (2016).
- 635 9. Burgess, D. J. Spatial transcriptomics coming of age. *Nat Rev Genet* **20**, 317 (2019).
- 636 10. Hardwick, S. A. *et al.* Single-nuclei isoform RNA sequencing unlocks barcoded exon
connectivity in frozen brain tissue. *Nature biotechnology* **40**, 1082–1092 (2022).
- 637 11. Hawrylycz, M. *et al.* A guide to the BRAIN initiative cell census network data
ecosystem. *PLoS biology* **21**, e3002133 (2023).
- 638 12. Wang, Q. *et al.* The allen mouse brain common coordinate framework: A 3D reference
atlas. *Cell* **181**, 936–953.e20 (2020).
- 639 13. Perens, J. *et al.* An optimized mouse brain atlas for automated mapping and quantifi-
cation of neuronal activity using iDISCO+ and light sheet fluorescence microscopy.
Neuroinformatics **19**, 433–446 (2021).
- 640 14. Ma, Y. *et al.* A three-dimensional digital atlas database of the adult C57BL/6J mouse
brain by magnetic resonance microscopy. *Neuroscience* **135**, 1203–1215 (2005).

- 641 15. Qu, L. *et al.* Cross-modal coherent registration of whole mouse brains. *Nature Methods* **19**, 111–118 (2022).
- 642 16. Kronman, F. N. *et al.* [Developmental mouse brain common coordinate framework](#). *Nat Commun* **15**, 9072 (2024).
- 643 17. Chuang, N. *et al.* An MRI-based atlas and database of the developing mouse brain. *Neuroimage* **54**, 80–89 (2011).
- 644 18. Dries, R. *et al.* Advances in spatial transcriptomic data analysis. *Genome research* **31**, 1706–1718 (2021).
- 645 19. Ricci, P. *et al.* Removing striping artifacts in light-sheet fluorescence microscopy: A review. *Progress in biophysics and molecular biology* **168**, 52–65 (2022).
- 646 20. Agarwal, N., Xu, X. & Gopi, M. Robust registration of mouse brain slices with severe histological artifacts. in *Proceedings of the tenth indian conference on computer vision, graphics and image processing* 1–8 (2016).
- 647 21. Agarwal, N., Xu, X. & Gopi, M. Automatic detection of histological artifacts in mouse brain slice images. in *Medical computer vision and bayesian and graphical models for biomedical imaging: MICCAI 2016 international workshops, MCV and BAMBI, athens, greece, october 21, 2016, revised selected papers* 8 105–115 (Springer, 2017).
- 648 22. Tward, D. *et al.* 3d mapping of serial histology sections with anomalies using a novel robust deformable registration algorithm. in *International workshop on multimodal brain image analysis* 162–173 (Springer, 2019).
- 649 23. Cahill, L. S. *et al.* Preparation of fixed mouse brains for MRI. *Neuroimage* **60**, 933–939 (2012).
- 650 24. Sunkin, S. M. *et al.* Allen brain atlas: An integrated spatio-temporal portal for exploring the central nervous system. *Nucleic acids research* **41**, D996–D1008 (2012).
- 651 25. Kim, Y. *et al.* Brain-wide maps reveal stereotyped cell-type-based cortical architecture and subcortical sexual dimorphism. *Cell* **171**, 456–469 (2017).
- 652 26. Fürth, D. *et al.* [An interactive framework for whole-brain maps at cellular resolution](#). *Nat Neurosci* **21**, 139–149 (2018).

- 653 27. Li, Y. *et al.* mBrainAligner-web: A web server for cross-modal coherent registration
of whole mouse brains. *Bioinformatics* **38**, 4654–4655 (2022).
- 654 28. Puchades, M. A., Csucs, G., Ledergerber, D., Leergaard, T. B. & Bjaalie, J. G. Spatial
registration of serial microscopic brain images to three-dimensional reference atlases
with the QuickNII tool. *PloS one* **14**, e0216796 (2019).
- 655 29. Eastwood, B. S. *et al.* Whole mouse brain reconstruction and registration to a
reference atlas with standard histochemical processing of coronal sections. *Journal of
Comparative Neurology* **527**, 2170–2178 (2019).
- 656 30. Ni, H. *et al.* A robust image registration interface for large volume brain atlas. *Sci
Rep* **10**, 2139 (2020).
- 657 31. Pallast, N. *et al.* Processing pipeline for atlas-based imaging data analysis of structural
and functional mouse brain MRI (AIDAmri). *Front Neuroinform* **13**, 42 (2019).
- 658 32. Celestine, M., Nadkarni, N. A., Garin, C. M., Bougacha, S. & Dhenain, M. **Sammba-
MRI: A library for processing SmAll-MaMmal BrAin MRI data in python**. *Front
Neuroinform* **14**, 24 (2020).
- 659 33. Ioanas, H.-I., Marks, M., Zerbi, V., Yanik, M. F. & Rudin, M. An optimized registration
workflow and standard geometric space for small animal brain imaging. *Neuroimage*
241, 118386 (2021).
- 660 34. Aggarwal, M., Zhang, J., Miller, M. I., Sidman, R. L. & Mori, S. Magnetic resonance
imaging and micro-computed tomography combined atlas of developing and adult
mouse brains for stereotaxic surgery. *Neuroscience* **162**, 1339–1350 (2009).
- 661 35. Chandrashekhar, V. *et al.* CloudReg: Automatic terabyte-scale cross-modal brain
volume registration. *Nature methods* **18**, 845–846 (2021).
- 662 36. Jin, M. *et al.* SMART: An open-source extension of WholeBrain for intact mouse
brain registration and segmentation. *eNeuro* **9**, (2022).
- 663 37. Negwer, M. *et al.* FriendlyClearMap: An optimized toolkit for mouse brain mapping
and analysis. *Gigascience* **12**, (2022).
- 664 38. Lin, W. *et al.* Whole-brain mapping of histaminergic projections in mouse brain.
Proceedings of the National Academy of Sciences **120**, e2216231120 (2023).

- 665 39. Zhang, M. *et al.* Spatially resolved cell atlas of the mouse primary motor cortex by MERFISH. *Nature* **598**, 137–143 (2021).
- 666 40. Shi, H. *et al.* Spatial atlas of the mouse central nervous system at molecular resolution. *Nature* **622**, 552–561 (2023).
- 667 41. Zhang, Y. *et al.* Reference-based cell type matching of *in situ* image-based spatial transcriptomics data on primary visual cortex of mouse brain. *Scientific Reports* **13**, 9567 (2023).
- 668 42. Klein, S., Staring, M., Murphy, K., Viergever, M. A. & Pluim, J. P. W. [Elastix: A toolbox for intensity-based medical image registration](#). *IEEE Trans Med Imaging* **29**, 196–205 (2010).
- 669 43. Fedorov, A. *et al.* 3D slicer as an image computing platform for the quantitative imaging network. *Magnetic resonance imaging* **30**, 1323–1341 (2012).
- 670 44. Tustison, N. J. *et al.* [The ANTsX ecosystem for quantitative biological and medical imaging](#). *Sci Rep* **11**, 9068 (2021).
- 671 45. Rolfe, S. M., Whikehart, S. M. & Maga, A. M. [Deep learning enabled multi-organ segmentation of mouse embryos](#). *Biol Open* **12**, bio059698 (2023).
- 672 46. Pagani, M., Damiano, M., Galbusera, A., Tsafaris, S. A. & Gozzi, A. Semi-automated registration-based anatomical labelling, voxel based morphometry and cortical thickness mapping of the mouse brain. *Journal of neuroscience methods* **267**, 62–73 (2016).
- 673 47. Anderson, R. J. *et al.* [Small animal multivariate brain analysis \(SAMBA\) - a high throughput pipeline with a validation framework](#). *Neuroinformatics* **17**, 451–472 (2019).
- 674 48. Allan Johnson, G. *et al.* Whole mouse brain connectomics. *Journal of Comparative Neurology* **527**, 2146–2157 (2019).
- 675 49. Yao, Z. *et al.* [A high-resolution transcriptomic and spatial atlas of cell types in the whole mouse brain](#). *Nature* **624**, 317–332 (2023).

- 676 50. Avants, B. B., Epstein, C. L., Grossman, M. & Gee, J. C. [Symmetric diffeomorphic](#)
image registration with cross-correlation: Evaluating automated labeling of elderly
and neurodegenerative brain. *Med Image Anal* **12**, 26–41 (2008).
- 677 51. Tustison, N. J. *et al.* [N4ITK: Improved N3 bias correction](#). *IEEE Trans Med Imaging*
29, 1310–20 (2010).
- 678 52. Bajcsy, R. & Broit, C. Matching of deformed images. in *Sixth International Conference*
on Pattern Recognition (ICPR'82) 351–353 (1982).
- 679 53. Bajcsy, R. & Kovacic, S. [Multiresolution elastic matching](#). *Computer Vision, Graphics,*
and Image Processing **46**, 1–21 (1989).
- 680 54. Gee, J. C., Reivich, M. & Bajcsy, R. [Elastically deforming 3D atlas to match anatomical](#)
[brain images](#). *J Comput Assist Tomogr* **17**, 225–36 (1993).
- 681 55. Klein, A. *et al.* [Evaluation of 14 nonlinear deformation algorithms applied to human](#)
[brain MRI registration](#). *Neuroimage* **46**, 786–802 (2009).
- 682 56. Murphy, K. *et al.* [Evaluation of registration methods on thoracic CT: The EMPIRE10](#)
[challenge](#). *IEEE Trans Med Imaging* **30**, 1901–20 (2011).
- 683 57. Baheti, B. *et al.* [The brain tumor sequence registration challenge: Establishing](#)
correspondence between pre-operative and follow-up MRI scans of diffuse glioma
patients. (2021).
- 684 58. Avants, B. B. *et al.* [The optimal template effect in hippocampus studies of diseased](#)
[populations](#). *Neuroimage* **49**, 2457–66 (2010).
- 685 59. Avants, B. B., Tustison, N. J., Wu, J., Cook, P. A. & Gee, J. C. [An open source](#)
[multivariate framework for n-tissue segmentation with evaluation on public data](#).
Neuroinformatics **9**, 381–400 (2011).
- 686 60. Manjón, J. V., Coupé, P., Martí-Bonmatí, L., Collins, D. L. & Robles, M. [Adaptive](#)
[non-local means denoising of MR images with spatially varying noise levels](#). *J Magn*
Reson Imaging **31**, 192–203 (2010).
- 687 61. Wang, H. *et al.* [Multi-atlas segmentation with joint label fusion](#). *IEEE Trans Pattern*
Anal Mach Intell **35**, 611–23 (2013).

- 688 62. Tustison, N. J. *et al.* Optimal symmetric multimodal templates and concatenated random forests for supervised brain tumor segmentation (simplified) with *ANTsR*. *Neuroinformatics* (2014) doi:[10.1007/s12021-014-9245-2](https://doi.org/10.1007/s12021-014-9245-2).
- 689 63. Tustison, N. J., Yang, Y. & Salerno, M. Advanced normalization tools for cardiac motion correction. in *Statistical atlases and computational models of the heart - imaging and modelling challenges* (eds. Camara, O. et al.) vol. 8896 3–12 (Springer International Publishing, 2015).
- 690 64. McCormick, M., Liu, X., Jomier, J., Marion, C. & Ibanez, L. ITK: Enabling reproducible research and open science. *Front Neuroinform* **8**, 13 (2014).
- 691 65. Beg, M. F., Miller, M. I., Trouvé, A. & Younes, L. Computing large deformation metric mappings via geodesic flows of diffeomorphisms. *International Journal of Computer Vision* **61**, 139–157 (2005).
- 692 66. Tustison, N. J. & Avants, B. B. Explicit B-spline regularization in diffeomorphic image registration. *Front Neuroinform* **7**, 39 (2013).
- 693 67. Hsu, L.-M. *et al.* CAMRI mouse brain MRI data.
- 694 68. Reshetnikov, V. *et al.* High-resolution MRI data of brain C57BL/6 and BTBR mice in three different anatomical views.
- 695 69. Rahman, N., Xu, K., Budde, M. D., Brown, A. & Baron, C. A. A longitudinal microstructural MRI dataset in healthy C57Bl/6 mice at 9.4 tesla. *Sci Data* **10**, 94 (2023).
- 696 70. Liu, J. *et al.* Concordance of MERFISH spatial transcriptomics with bulk and single-cell RNA sequencing. *Life Sci Alliance* **6**, (2023).
- 697 71. Stringer, C., Wang, T., Michaelos, M. & Pachitariu, M. Cellpose: A generalist algorithm for cellular segmentation. *Nat Methods* **18**, 100–106 (2021).
- 698 72. Jia, H., Yap, P.-T., Wu, G., Wang, Q. & Shen, D. Intermediate templates guided groupwise registration of diffusion tensor images. *NeuroImage* **54**, 928–939 (2011).
- 699 73. Tang, S., Fan, Y., Wu, G., Kim, M. & Shen, D. RABBIT: Rapid alignment of brains by building intermediate templates. *NeuroImage* **47**, 1277–1287 (2009).

- 700 74. Dewey, B. E., Carass, A., Blitz, A. M. & Prince, J. L. Efficient multi-atlas registration
using an intermediate template image. in *Proceedings of SPIE—the international society
for optical engineering* vol. 10137 (NIH Public Access, 2017).
- 701 75. Perens, J. *et al.* Multimodal 3D mouse brain atlas framework with the skull-derived
coordinate system. *Neuroinformatics* **21**, 269–286 (2023).
- 702 76. Rotolo, T., Smallwood, P. M., Williams, J. & Nathans, J. Genetically-directed, cell
type-specific sparse labeling for the analysis of neuronal morphology. *PLoS One* **3**,
e4099 (2008).
- 703 77. Peng, H. *et al.* Morphological diversity of single neurons in molecularly defined cell
types. *Nature* **598**, 174–181 (2021).
- 704 78. Gong, H. *et al.* High-throughput dual-colour precision imaging for brain-wide connec-
tome with cytoarchitectonic landmarks at the cellular level. *Nat Commun* **7**, 12142
(2016).
- 705 79. Wang, J. *et al.* Divergent projection patterns revealed by reconstruction of individual
neurons in orbitofrontal cortex. *Neurosci Bull* **37**, 461–477 (2021).
- 706 80. Kronman, F. A. *et al.* Developmental mouse brain common coordinate framework.
bioRxiv (2023) doi:[10.1101/2023.09.14.557789](https://doi.org/10.1101/2023.09.14.557789).
- 707 81. Chon, U., Vanselow, D. J., Cheng, K. C. & Kim, Y. Enhanced and unified anatomical
labeling for a common mouse brain atlas. *Nat Commun* **10**, 5067 (2019).
- 708 82. Tasic, B. *et al.* Adult mouse cortical cell taxonomy revealed by single cell transcript-
omics. *Nat Neurosci* **19**, 335–46 (2016).
- 709 83. Bergmann, E., Gofman, X., Kavushansky, A. & Kahn, I. Individual variability in
functional connectivity architecture of the mouse brain. *Commun Biol* **3**, 738 (2020).
- 710 84. Billot, B. *et al.* SynthSeg: Segmentation of brain MRI scans of any contrast and
resolution without retraining. *Med Image Anal* **86**, 102789 (2023).
- 711 85. Tustison, N. J. & Amini, A. A. Biventricular myocardial strains via nonrigid registration
of anatomical NURBS model [corrected]. *IEEE Trans Med Imaging* **25**, 94–112 (2006).
- 712 86. Avants, B. B. *et al.* The Insight ToolKit image registration framework. *Front Neu-
roinform* **8**, 44 (2014).

- ⁷¹³ 87. Falk, T. *et al.* U-net: Deep learning for cell counting, detection, and morphometry. *Nat Methods* **16**, 67–70 (2019).
- ⁷¹⁴ 88. Tustison, N. J. *et al.* Image- versus histogram-based considerations in semantic segmentation of pulmonary hyperpolarized gas images. *Magn Reson Med* **86**, 2822–2836 (2021).